SAND2015-4185J

Investigation of the Dynamic Stress-Strain Response of Compressible Polymeric Foam Using an Inverse Analysis

Behrad Koohbor[1], Addis Kidane[1*], Wei-Yang Lu[2], Michael A. Sutton[1]

1. Department of Mechanical Engineering, University of South Carolina, 300 Main Street, Columbia, SC 29208
2. Sandia National Laboratories, Livermore, CA 94551-0969, USA

Abstract

Dynamic stress-strain response of rigid closed-cell polymeric foams exposed to direct impact loading is investigated in this work by subjecting high toughness polyurethane foam specimens to direct impact with different projectile velocities and quantifying their deformation response with high speed stereo-photography together with 3D digital image correlation. The measured transient displacement field developed in the specimens during high stain rate loading is used to calculate the transient axial acceleration field throughout the specimen. A simple mathematical formulation based on conservation of mass is also proposed to determine the local change of density in the specimen during deformation. By obtaining the full-field acceleration and density distributions, the inertia stresses at each point in the specimen are determined through an inverse analysis process and superimposed on the stress magnitudes measured at specimen ends, to obtain the full-field stress distribution. The process outlined above overcomes a major challenge in high strain rate experiments with low impedance polymeric foam specimens, i.e. the delayed dynamic equilibrium conditions can be quantified.

Keywords: Polymeric Foam; Direct Impact; Digital Image Correlation; Inverse Analysis, Parameter Identification

* Corresponding Author
Email: kidanea@cec.sc.edu
Address: Department of Mechanical Engineering, University of South Carolina, 300 Main Street, Columbia, South Carolina, 29208 | Tel: +1 (803) 777 2502 | Fax: +1 (803) 777 0106

1. Introduction

Determination of a material's constitutive behavior at intermediate to high strain rate ranges has been a subject of interest for quite a long time [1, 2]. Historically, the importance of obtaining dynamic equilibrium has required special attention in the experimental setup, since configurations where dynamic equilibrium can be readily identified make it easier to study the dynamic stress-strain response of the materials. The issue is particularly significant in the case of engineering materials with low strength and low mechanical impedance [3], where conditions of stress/strain equilibrium oftentimes require a time duration that exceeds the time required for the material to undergo failure. In such cases, the determination of stress-strain response of the material based on the load and displacement measurement at specimen ends can introduce a significant degree of inaccuracy in the obtained constitutive response, with continued deterioration in accuracy at higher strain rates [4-6].

Polymeric foams, materials widely used in applications which require light weight structural design with superior energy dissipation characteristics, are among the materials possessing a low wave propagation speed [7-10]. Their application in areas such as automotive industries, ships and packaging requires precise knowledge of the deformation response of the material at different loading rates. Dynamic deformation and failure behavior of these materials have been studied both experimentally and numerically in recent years [11-16]. In general, most polymeric foams possess remarkable strain rate sensitivity at strain rates above 500 s^{-1} [14]. However, owing to non-homogeneity in the stress and deformation states, particularly during the early stages of dynamic loading, quantifying the dynamic deformation of foams has been a major challenge. One of the most widely used methods in studying the dynamic deformation behavior of soft materials is the split Hopkinson pressure bar technique [17]. Different approaches have been practiced in recent years to increase the accuracy of the measurements in this technique. These approaches include pulse shaping techniques [17], use

of polymeric bars [18] and long projectiles [19], etc. A recent study by Liu et al. [16] indicates that in addition to the solutions proposed above, full-field measurements must be incorporated in order to accurately measure the deformation response and reveal the active failure mechanisms in foam specimens subjected to high strain rate loading conditions.

The advent of full-field measurement techniques such as Digital image correlation (DIC), in conjunction with different experimental techniques has facilitated the study of deformation of materials in a wide range of time and length scales [16, 20-24]. More importantly, the recent work by Pierron and his group [21, 25, 26] using virtual fields and inverse methods has identified a unique way of analyzing the dynamic deformation of materials by using D'Alembert's principle and incorporating "inertia forces" into the analysis. Though the inverse methods have already been demonstrated to be effective in calculating the stress-stress response of materials at high strain rate loading conditions, the effect of compressibility has not been addressed in previous studies.

The present work focuses on the study of rigid closed-cell polymeric foams subjected to direct impact loading by accounting for material compressibility and the effect of inertia. A shock tube apparatus is used to apply dynamic loading on the foam specimens, while high speed stereovision imaging together with 3D digital image correlation is used to study the full-field deformation of the material under high strain rate loading conditions. A simple mathematical model has also been proposed to account for the material compressibility and the local variation of density during deformation of the specimens. Also, based on the full-field displacement distribution captured by DIC and considering the instantaneous change of material density, an inverse analysis process was developed to incorporate "inertia effects" into the analysis. Using the proposed methodology, the full-field stress-strain response of the material has been determined during high strain rate loading and the global constitutive behavior of the foam quantified. To the authors' knowledge, this is the first time a thorough

analysis of the dynamic deformation of compressible polymeric foams has been performed taking into account the concurrent effects of material compressibility and inertia loading to capture the full-field stress-strain response of the material.

2. Experimental Procedure

2.1. Material and Specimen Geometry

The material used in this study is a rigid closed-cell polyurethane foam of 560 kg/m^3 (35 pcf) nominal density obtained from Sandia National Laboratories [27]. The initial density of the foam specimens was measured in-house and confirmed to be consistent with density values reported in the literature [27]; the measured value was 95% of literature data. A cylindrical foam specimen with a high contrast speckle pattern is shown in Figure 1a. The specimen is 25.4 mm in diameter and 25.4 mm in height. Each specimen was extracted from the as-received billets using a waterjet system, resulting in a relatively smooth lateral surface finish with +/- 0.1 mm dimensional variability. The high contrast speckle pattern shown in Figure 1a consists of a thin white sub-layer with randomly-distributed black speckles; the black speckles were applied using an airbrush. A histogram of the speckle pattern is shown in Figure 1b.

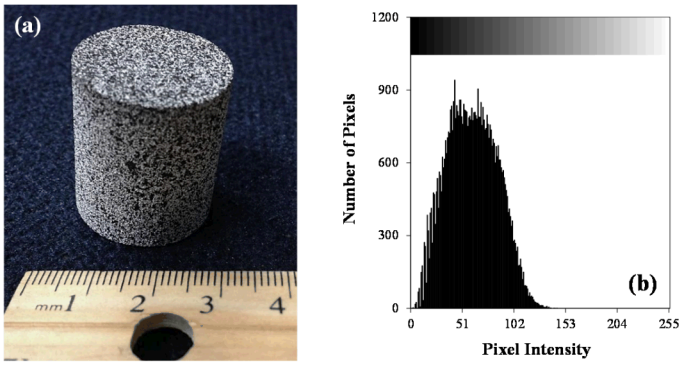

Fig. 1- (a) Typical speckled specimen with its corresponding grey scale histogram shown in (b).

2.2. Impact Loading

A shock tube apparatus was utilized to apply controlled dynamic loading on the specimens. The shock tube used in this work is shown in Figure 2a. The apparatus has an overall length of 7.2 m, consisting of a 1.8 m driven section and a 5.4 m driver section. The inner diameter of the entire tube, except the last 0.9 m section near to the muzzle, is 75 mm. The inner diameter of the final 0.9 m end section of the tube is 50 mm, resulting in increasing shock velocity over the final stage.

To perform the experiment, the speckled cylindrical specimen shown in Figure 1a is placed at the muzzle of the shock tube and affixed to a custom fabricated strong-back. As shown in Figure 2b, three piezotronic load-cells were placed behind the specimen and mounted on a specially fabricated fixture. Use of three load-cells in this work assures the accuracy of the measurements and compensates for any possible misalignment of the loading which might occur during high strain rate experiments. The specimen is held on the loading fixture by the use of lithium grease, which also acts as the lubricant. Further details on the shock tube used in this work can be found elsewhere [4, 24, 28, 29].

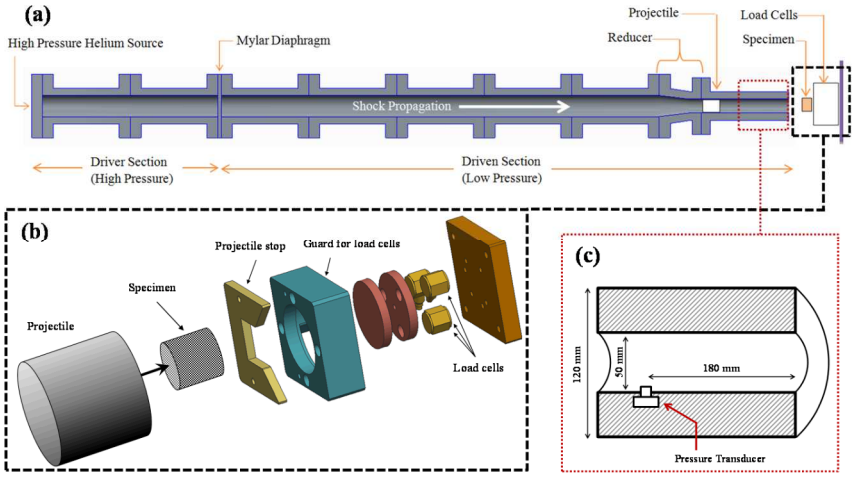

Fig. 2- (a) The shock tube at its entirety, with the loading fixture shown in (b). The schematic of the shock tube muzzle and the pressure transducer are depicted in (c).

As shown in Figure 2b, direct impact loading is applied using a projectile placed inside the tube at the beginning of the reducing section. The projectile was made of high strength 7068 aluminum alloy with a diameter 2 mm smaller than the inside diameter of the reducing section. The projectile was fabricated as a cylinder hollowed from one end, to reduce its mass, with an overall length of 72 mm, and a 0.07 kg mass. Prior to performing the experiment, the high pressure driver section and the low pressure driven section are separated by a diaphragm, a 0.18 mm thick stretched polyester film, under the commercial name Mylar. During testing, the driver section is pressurized using helium gas and as the pressure difference reaches a critical value, the polyester film bursts, forming a shock wave that pushes the projectile towards the specimen side. The pressure and the velocity of the shock and the associated strain rate can be manipulated by varying the number of diaphragms separating the driven and driver sections. In this work, two different strain rates were successfully applied on the specimen by using one and two sheets of diaphragms. The pressure profile developed inside the shock tube was measured using a piezotronic pressure sensor placed inside the tube near to the muzzle (See Figure 2c). Maximum internal pressures of 250 kPa and 350 kPa were accordingly measured, by using one and two Mylar sheets, respectively.

Upon the formation of the shock inside the shock tube, the projectile is shot directly at the specimen, imposing a large strain rate magnitude on the deforming material. Stereo-imaging of the specimen was performed using two Photron SAX-2 high speed cameras. Triggering of the cameras was facilitated using the pressure transducer located inside and 180 mm behind the muzzle outlet of the tube (See Figure 2c). The pressure transducer was connected to the oscilloscope so that the signal from the transducer can be used to trigger the cameras as the internal pressure increased inside the tube. Repeatability of the results obtained from dynamic tests in this work was assured by testing two specimens for each strain rate conditions.

2.3. Imaging Setup and Digital Image Correlation

The pair of Photron SAX-2 cameras used in these studies are equipped with 100 mm lenses. Images were acquired at a rate of 10^5 fps at 384×264 pix^2 full-field resolutions resulting in inter-frame intervals of 10 μs. The load-cell data acquisition rate was synchronized with the imaging rate through a high speed data acquisition system and an oscilloscope.

Images acquired during the specimen deformation period were used as the input to the commercial DIC software Vic-3D® for quantitative 3D digital image correlation analysis. In this software, subset and step sizes of 39 pix and 9 pix were selected, respectively; the resolution of the measurements was calculated as ~9.16 pix/mm. Further details of the stereovision camera system parameters are listed in Table 1. The experimental setup including the shock tube and the stereovision camera arrangement system used in this work is shown in Figure 3.

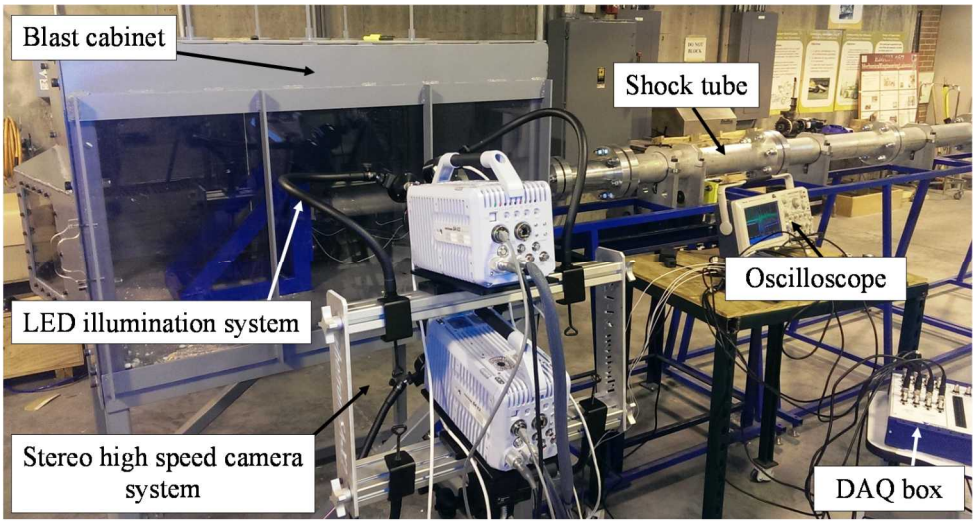

Fig. 3- The experimental setup including the shock tube and the stereovision camera system used in this work.

Table 1- System parameters obtained from calibration of the stereo camera arrangements used in this work

Parameter		Camera 1	Camera 2
Center - x	(pix)	148.7	167.5
Center - y	(pix)	24.2	43.9
Focal length - x	(pix)	5799.5	5708.3
Focal length - y	(pix)	5796.1	5705.3
Skew	(°)	-0.89	-0.48
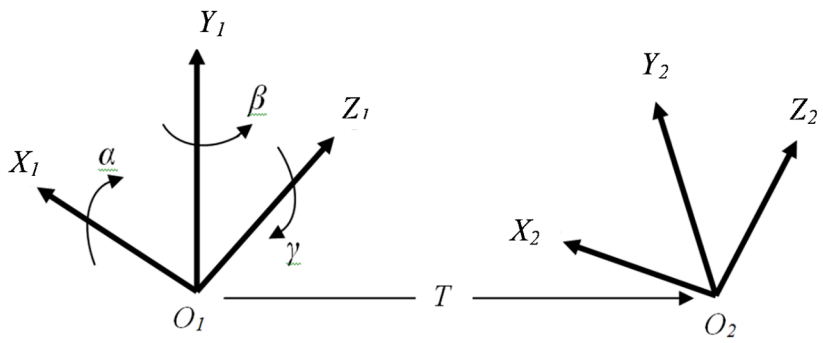			
Alpha	(°)	20.6	
Beta	(°)	-0.8	
Gamma	(°)	-0.6	
Tx	(mm)	6.8	
Ty	(mm)	223.7	
Tz	(mm)	41.9	

3. Data Analysis

3.1. Modeling of Material Compressibility

The polymeric foam specimens examined in this work are compressible, and hence their density varies when subjected to deformation [30]. To take the material compressibility into account, a simple one-dimensional model was proposed in this work, which facilitates the calculation of material's instantaneous density, as a function of its initial density and the applied strain components.

Consider a compressible cylindrical specimen of initial volume Ω_0 and initial density ρ_0, exposed to axial compression from one side, and deformed into a cylinder of volume Ω, and density ρ at time t, as schematically shown in Figure 4. The temporal rate of change of the specimen volume, $\dot{\Omega}$, can be written as:

$$\frac{\dot{\Omega}}{\Omega} = 2\frac{\dot{r}}{r} + \frac{\dot{h}}{h} \tag{1}$$

Where $\dot{r}$ and $\dot{h}$ are the temporal rate of change of radius and height of the cylindrical specimen, respectively. Assuming logarithmic strain metrics for both the radial and axial strain components, and the apparent plastic Poisson's ratio as υ_p, the strain rate equations can be written;

$$\dot{\varepsilon}_r = \frac{\dot{r}}{r} \qquad \dot{\varepsilon}_z = \frac{\dot{h}}{h} \tag{2a}$$

$$\dot{\varepsilon}_r = -\upsilon_p \dot{\varepsilon}_z \tag{2b}$$

Thus, Eq. (1) can be written in the following form;

$$\frac{\dot{\Omega}}{\Omega} = \left(1 - 2\upsilon_p\right)\dot{\varepsilon}_z \tag{3}$$

Eq. (3) can be further simplified by defining the instantaneous axial strain rate as [31]:

$$\dot{\varepsilon}_z = -\frac{V}{h} \tag{4}$$

where V is the magnitude of the velocity of the specimen at its free surface and h denotes the instantaneous specimen height, as shown schematically in Figure 4. Note that the definition of the axial strain rate in Eq. (4) requires that the velocity, V, remains constant throughout the entire duration of the specimen deformation. The form shown in Eq. (4) was investigated

through 3D DIC analysis of multiple foam impact experiments, and it was confirmed that the velocity of the specimen surface at the projectile side remains constant during deformation, as described in detail in the following sections. Using Eqs. (3) and (4), the rate of change of the specimen volume can be rewritten in terms of the plastic Poisson's ratio and the free end velocity, as:

$$\frac{\dot{\Omega}}{\Omega} = \left(2\upsilon_p - 1\right)\frac{V}{h} \tag{5}$$

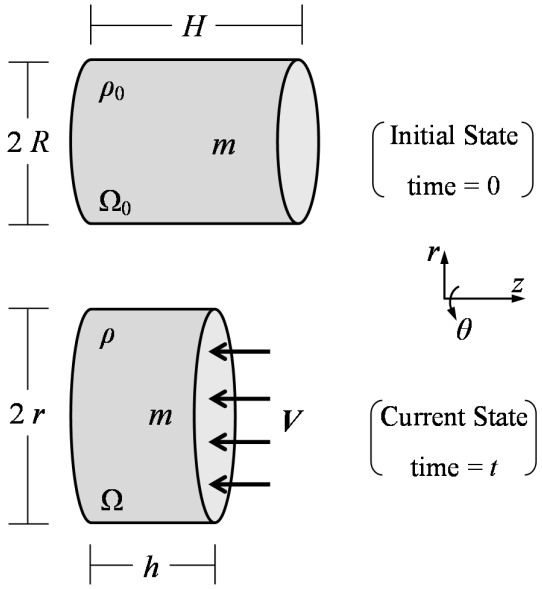

Fig. 4- The schematic view of a compressible cylindrical specimen subjected to axial loading.

Now, by considering the principle of conservation of mass for the compressible cylindrical specimen shown in Figure 4, the rate of change in density can be written as:

$$\dot{\rho} = -\left(\frac{\dot{\Omega}}{\Omega}\right)\rho \tag{6}$$

Assuming that the density, ρ, varies only along the z-direction and applying a simple mathematical chain rule, Eq. (6) can be rewritten as:

$$\frac{d\rho}{dh}\cdot\frac{dh}{dt}=-\left(\frac{\dot{\Omega}}{\Omega}\right)\rho \tag{7}$$

where by defining $\frac{dh}{dt}=-V$ and upon rearrangement, the final ordinary differential equation can be obtained as:

$$\frac{d\rho}{\rho}=\left(2\upsilon_p-1\right)\frac{dh}{h} \tag{8}$$

Eq. (8) can be integrated to yield:

$$\rho=\rho_0\left(\frac{h}{H}\right)^{2\upsilon_p-1} \tag{9}$$

Also, Eq. (9) can be written in terms of the axial strain, $\varepsilon_z=\ln\left(\frac{h}{H}\right)$, as:

$$\rho=\rho_0\left[\exp\left(\varepsilon_z\right)\right]^{2\upsilon_p-1} \tag{10}$$

The significance of Eqs. (9) and (10) is that the variables h, ε_z and υ_p can be experimentally measured using digital image correlation at any given point along the specimen axis. The plastic Poisson's ratio, υ_p, can be measured for a cylindrical specimen as the ratio between the radial and axial strain components. In this work, to measure the local evolution of υ_p, a cylindrical coordinate system was first assigned to the initial geometry of the specimen. Then, by tracking the evolution of the radial displacement component during the entire time of deformation, the radial strain component was determined. The plastic Poisson's ratio also was calculated over the entire region of interest. Finally, it should be noticed that the

mathematical expression shown in Eq. (10) predicts perfect incompressibility when $\upsilon_p = 0.5$, i.e. the condition existing in the plastic deformation of perfectly plastic materials, e.g. metals.

3.2. Dynamic Stress-Strain Response Using an Inverse Method

In order to include the roles of inertia force and stress in the measurements in this work, an inverse analysis was performed in which the inertia stress within the specimen was reconstructed using the full-field deformation response of the foam specimen during dynamic loading.

Consider a cylindrical specimen, schematically shown in Figure 5, subjected to direct impact load on its right end exerted by a projectile. The load-cell is located at the opposite side of the specimen. Let Ω be the current domain of interest. Each point inside the domain is represented by a position vector $\underline{z} = z_1\underline{e}_1 + z_2\underline{e}_2 + z_3\underline{e}_3$ in the domain. The force applied at any given position along the specimen axis $\underline{z}$ and at time *t* can be expressed as:

$$\underline{F}(\underline{z},t) = F_1(z_1,t)\underline{e}_1 \tag{11}$$

Considering the free body diagram of the sliced section in Figure 5 and applying Newton's law of motion in e_1-direction, the following equation can be written:

$$F_1(z_1 + dz,t) - F_1(z_1,t) = \rho(z_1,t)A(z_1,t)\,dz_1\,\frac{\partial^2 u_1}{\partial t^2}(z_1,t) \tag{12}$$

where $\rho(z_1,t)$ and $A(z_1,t)$ are specimen density and cross sectional area at position z_1 and time *t*, respectively. Also, $u_1(z_1,t)$ represents the displacement component along the e_1-direction. Eq. (12) can be rewritten in differential from as:

$$\frac{\partial F_1}{\partial z_1}(z_1,t) = \rho(z_1,t)A(z_1,t)\frac{\partial^2 u_1}{\partial t^2}(z_1,t) \tag{13}$$

which upon integration yields:

$$F_1(z_1,t) = F_1(0,t) + \int_{\xi=0}^{\xi=z_1} \rho(\xi,t) A(\xi,t) \frac{\partial^2 u_1}{\partial t^2}(\xi,t)\, d\xi \tag{14}$$

Note that Eq. (14) indicates that the force at any position $z = z_1$ can be reconstructed from the force at position $z = 0$, i.e. at the location of the load-cells, along with the acceleration and density at position $z = z_1$. The density component at any location can be obtained using the equations described in section 3.1. The acceleration component at any given position along the e_1-direction can also be calculated from the displacement field obtained from DIC. In this work, a central difference scheme was utilized to numerically calculate the full-field acceleration distribution within the deforming specimen. Accordingly, the acceleration component $a_1(z_1,t) = \frac{\partial^2 u_1}{\partial t^2}(z_1,t)$ was calculated as:

$$a_1(z_1,t) = \frac{1}{\Delta t^2}\left[u_1(z_1, t-\Delta t) - 2u_1(z_1,t) + u_1(z_1, t+\Delta t)\right] \tag{15}$$

where Δt denotes the time interval between two consecutive images, i.e. Δt=1/(frame rate).

Similar to Eq. (14), the stress component in e_1-direction can be recovered as:

$$\sigma_1(z_1,t) = \frac{F_1(0,t)}{A(z_1,t)} + \int_{\xi=0}^{\xi=z_1} \rho(\xi,t) \frac{\partial^2 u_1}{\partial t^2}(\xi,t)\, d\xi \tag{16}$$

The stress component $\sigma_1(z_1,t)$ can be inversely calculated from the stress magnitude measured at the load-cell side plus the inertia stress shown in integral term in Eq. (16).

Note that true stress value at any given position across the domain of interest can be calculated only if the current cross sectional area $A(z_1,t)$ at the same position is identified. As described in the previous section, the change of the cross section of the cylindrical specimen

can be measured directly from DIC. In this case also, a cylindrical coordinate system can be assigned on the initial configuration to facilitate measuring of the current dimensions of the cylindrical specimen at any given position in space and time.

By including compressibility of the foam into the analysis, the final closed form equation that can be used to reconstruct the axial stress at any given position across the domain of interest can be written as:

$$\sigma_1(z_1,t)=\frac{F_1(0,t)}{A(z_1,t)}+\int_{\xi=0}^{\xi=z_1}\rho_0\left[\exp\left(\varepsilon_z(\xi,t)\right)^{2\upsilon_p(\xi,t)-1}\right]\frac{\partial^2 u_1}{\partial t^2}(\xi,t)\,d\xi \tag{17}$$

Assuming that the deformation of the specimens takes is only axial, to calculate the stress using the full-field data extracted from DIC and Eq. (17), the cylindrical geometry of the specimen is sliced into a finite number of thin sections of thickness *s* along the specimen length. Then, density and acceleration values within each section are calculated by averaging these parameters over the entire volume of each thin sliced section. Now, the integral term on the right hand side of Eq. (16) can be approximated as:

$$\int_{\xi=0}^{\xi=z_1}\rho(\xi,t)\frac{\partial^2 u_1}{\partial t^2}(\xi,t)d\xi\approx\sum_{i=1}^{n}\rho^{(i)}a^{(i)}s^{(i)} \tag{18}$$

Where $\rho^{(i)}$ and $a^{(i)}$ are the local density and axial acceleration values at section *i*, respectively. $s^{(i)}$ represents the slice thickness, and *n* denotes the total number of sliced sections up to the location of z_1 (See Figure 6).

The deformation homogeneity in each case is investigated by defining the inhomogeneity coefficient for strain (α_{ε_1}) and stress (α_{σ_1}) as [5]:

$$\alpha_{\varepsilon_1}(t)=\sqrt{\frac{\int_0^h\left|\varepsilon_1(z,t)-\langle\varepsilon_1\rangle(t)\right|dz}{\int_0^h\left|\langle\varepsilon_1\rangle(t)\right|dz}} \tag{19a}$$

$$\alpha_{\sigma_1}(t)=\sqrt{\frac{\int_0^h\left|\sigma_1(z,t)-\langle\sigma_1\rangle(t)\right|dz}{\int_0^h\left|\langle\sigma_1\rangle(t)\right|dz}} \tag{19b}$$

where,

$$\langle\varepsilon_1\rangle(t)=\frac{1}{h}\left(\int_0^h\varepsilon_1(z,t)dz\right) \tag{20a}$$

$$\langle\sigma_1\rangle(t)=\frac{1}{h}\left(\int_0^h\sigma_1(z,t)dz\right) \tag{20b}$$

Note that $\langle\varepsilon_1\rangle(t)$ and $\langle\sigma_1\rangle(t)$ represent the spatial average value of the axial stress and axial strain at any given time *t*, respectively.

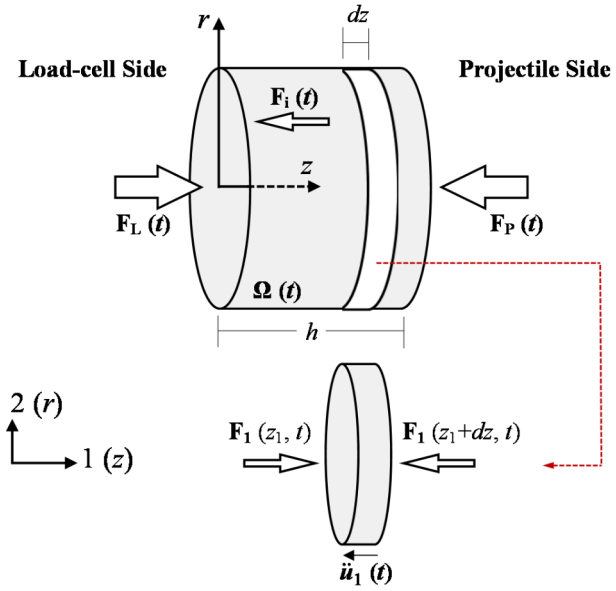

Fig. 5- Schematic of a cylindrical specimen subjected to direct impact. The dynamic load is applied on the specimen from the projectile side.

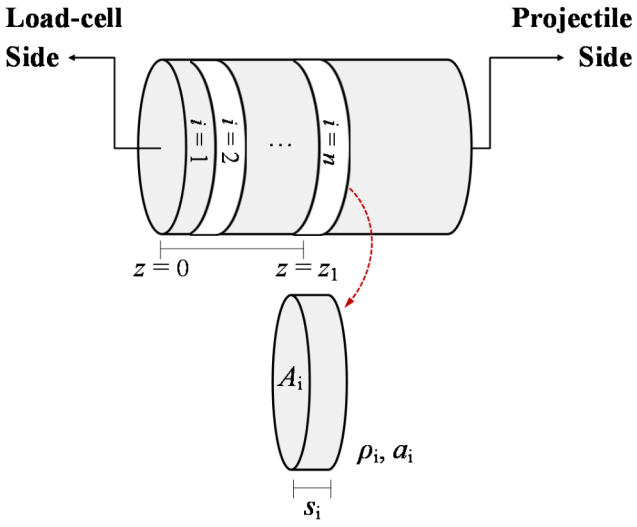

Fig. 6- Schematic geometry of the specimen sliced into a finite number of thinner segments, used to calculate the inertia force and stress applied at each point across the specimen axis.

4. Results and Discussion

Two different strain rates were applied in this work, associated with one and two Mylar sheets used to separate the driver and the driven sections of the shock tube. To calculate the average strain rate applied to the specimen, the axial strain magnitudes over the entire domain of interest were averaged and plotted as a function of deformation time, as shown in Figure 7. The slopes of the best linear fits are then considered as the average strain rate in each case. The average strain rates obtained through this procedure are 1437 s^{-1} and 2458 s^{-1} corresponding to one and two Mylar sheets, respectively. The error bars indicate the level of inhomogeneity of the strain fields at the corresponding applied strain. Considering the strain data shown in Figure 7, the level of inhomogeneity of axial strain is observed to be higher in higher strain rate condition. Furthermore, the strain inhomogeneity is found to be higher at earlier stages of deformation, i.e. the time during which dynamic equilibrium has not yet achieved. The full-field axial and radial strain components for the highest strain rate

condition are shown in Figure 8, confirming the above statements. Note that Figure 8 shows the inhomogeneity in the strain distribution for both axial and radial strain contours. As described earlier, the contours shown in Figure 8 were plotted by slicing the entire region of interest into 25 thinner slices of about 1 mm thickness, and averaging the strain components, extracted from DIC, over the entire volume of each slice.

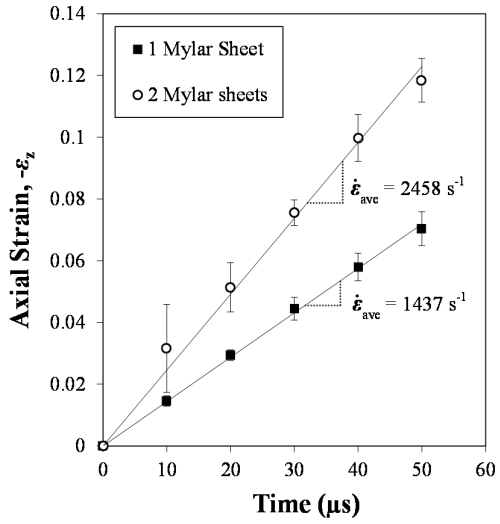

Fig. 7- Evolution of the average axial strain applied on the specimen as a functions of time, for two different number of Mylar sheets.

Using the obtained radial and axial strain distributions, evolution of the plastic Poisson's ratio in the region of interest was also determined. Contours showing the evolution of plastic Poisson's ratio for the specimen deformed under the higher strain rate conditions have been depicted in Figure 9. The evolution of υ_p at 3 different positions along the specimen axis has also been plotted in Figure 10, for both strain rate conditions. Larger plastic Poisson's ratio values were obtained for the specimen deformed under lower strain rate conditions, indicating that the foam specimens examined in this work experience a larger compressibility at higher strain rate (See Eq. (10)).

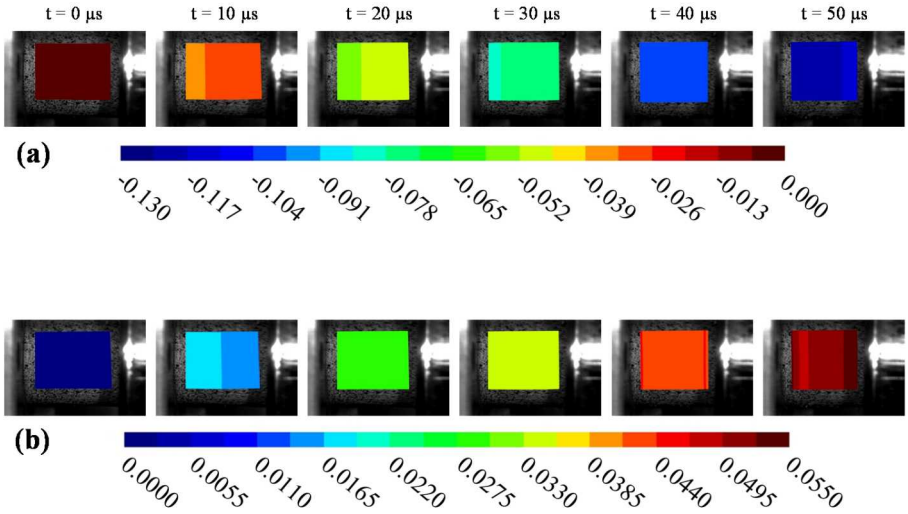

Fig. 8- full-field distribution of (a) axial and (b) radial strain components for the specimen subjected to direct impact with two Mylar sheets.

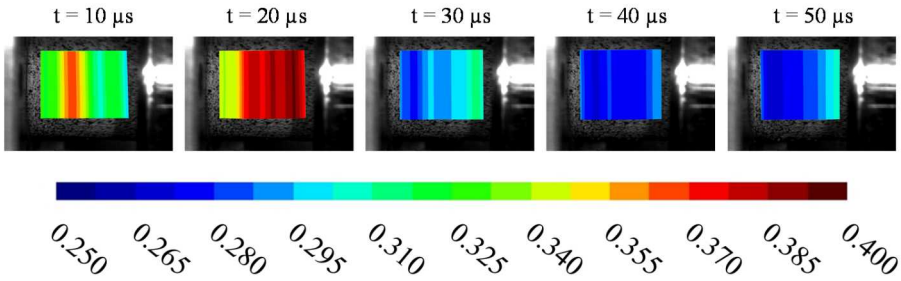

Fig. 9- full-field distribution of plastic Poisson's ratio, υ_p, for the specimen subjected to direct impact with two Mylar sheets.

Next, to calculate the change of density based on the mathematical model described earlier in Sec. 3.1, our assumption, i.e. the constant velocity of the projectile throughout the entire duration of the specimen deformation, must be satisfied. The displacement of the tip of the projectile with respect to time, measured from the high speed images, is shown in Figure 11.

The velocity of the projectile was calculated by differentiating the projectile displacement with respect to time and was shown to remain constant well after incidence with the specimen. In addition, experimental data confirms that the average projectile velocity increased by 35% when the number of mylar diaphragms increased from one to two.

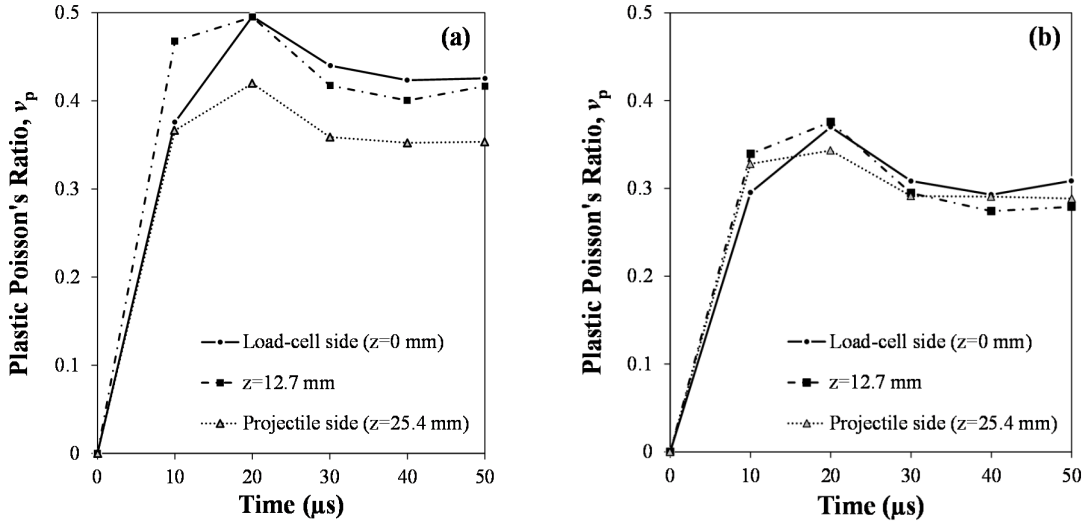

Fig. 10- Local plastic Poisson's ratio, v_p, of the specimens extracted from different positions along the axis of foam specimens deformed at (a) 1437 s^{-1} and (b) 2458 s^{-1} strain rates.

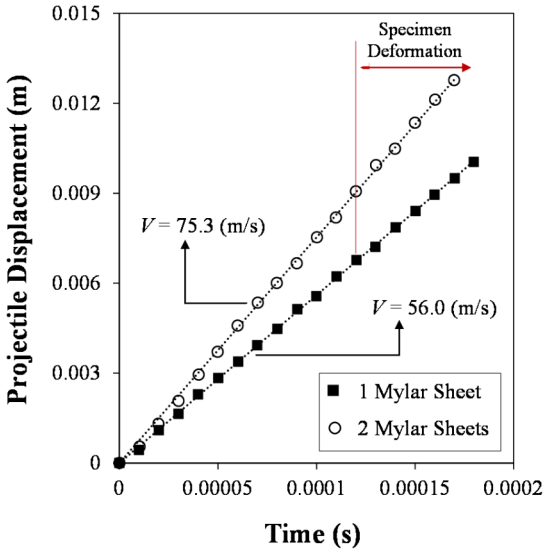

Fig. 11- Variation of the projectile displacement with time. Increasing the number of plastic diaphragms from one to two has resulted in a 35% increase in the velocity of the projectile.

The local change of density of the specimens at different strain rate conditions can be determined once (a) it has been shown that V = constant and (b) the evolution of the plastic Poisson ratio, υ_p, has been determined. Figure 12 illustrates the typical form obtained for the local change of density of the specimens at three different locations along the specimen axis. For the case of lower strain rate condition, the foam specimen shows less compressibility with a negligible (~2%) change of density (see Figure 12a). However, the density of the specimen changes more noticeably under higher strain rate conditions (> 5%), while υ_p deviates from a perfect plastic condition, i.e. $\upsilon_p = 0.5$. Based on these results, the change of density must be considered in the calculation of inertia forces and stresses developed within the specimen to increase the accuracy of the predictions. Note that the change of density calculated for materials considered in this work are relatively small. However, the proposed model can be used for any compressible solid, regardless of the degree of compressibility.

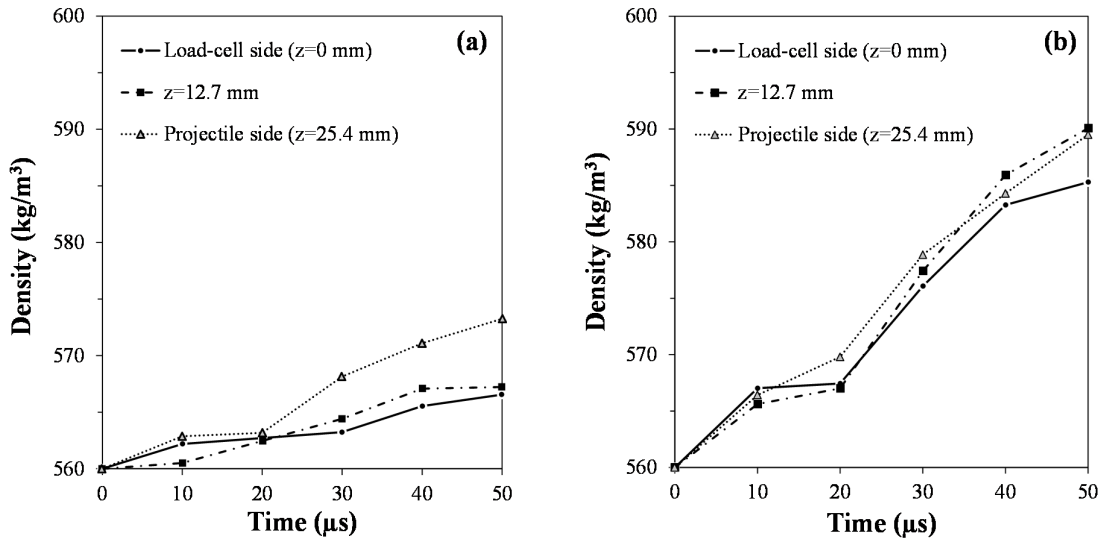

Fig. 12- variation of local density as a function of deformation time, extracted from different positions along the axis of foam specimens deformed at (a) 1437 s^{-1} and (b) 2458 s^{-1} strain rates.

The full-field acceleration distribution was calculated based on the procedure described in earlier sections. Full-field axial displacement and acceleration maps at each time step are shown in Figure 13 for the specimen subjected to higher strain rate conditions. Figure 13a shows a rather circumferentially-homogeneous distribution of the axial displacement. The axial acceleration, on the other hand, is distributed in a highly nonhomogeneous pattern, particularly in the earlier stages of deformation, i.e. $0 < t < 20$ μs (See Figure 13b). The axial acceleration then becomes smaller in magnitude and more homogeneous for longer durations, as shown in Figure 14, where the axial acceleration component was averaged over the entire domain of interest and plotted at each deformation time step. For both strain rate conditions, a sudden change in the magnitude of the average acceleration takes place at $t = 10$μs. The large magnitude of acceleration, as well as its level of discrepancy, is gradually decreased at later deformation stages. The large value of acceleration obtained in early stages of deformation results in a significant increase of inertia force and inertia stress (see Eqs. (14) to (17)) at earlier deformation times, as also reported previously in [5].

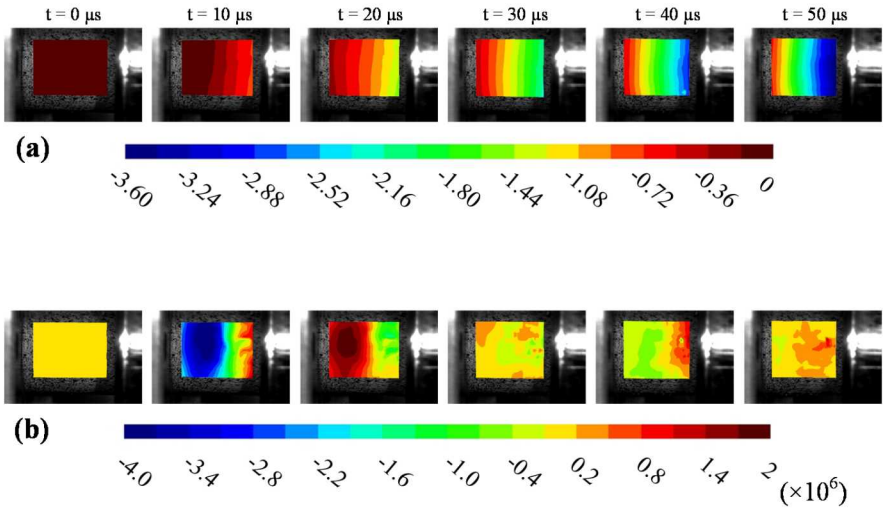

Fig. 13- full-field distribution of (a) axial displacment (mm) and (b) axial acceleration (m/s^2) for the specimen subjected to higher strain rate conditions.

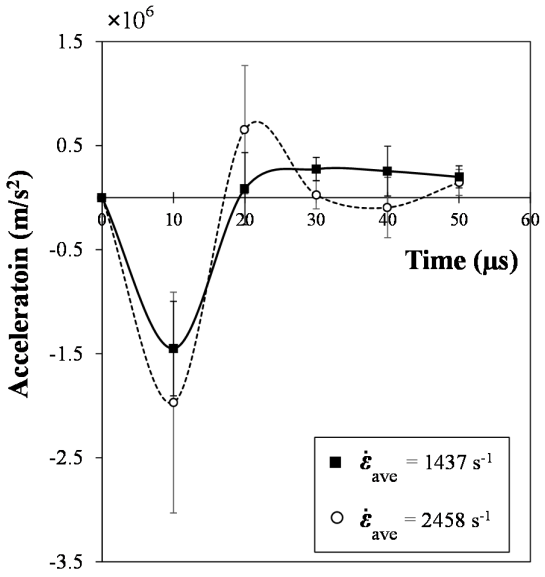

Fig. 14- Variation of the axial acceleration averaged over the entire domain of interest with respect to time.

Having obtained all the required parameters, the values of force and stress can be reconstructed at any given position along the specimen axis, following the procedure detailed in Sec.3.2. The force applied on the load-cell side of the specimen can be directly measured from the load-cells inserted behind the specimen. However, the force applied on the other side, i.e. the projectile side, is required to be inversely calculated using the load measured on the load-cell side along with the acceleration and density fields obtained earlier. The forces acting on two sides of the foam specimens are plotted in Figure 15. In both strain rate conditions, the load measured on the load-cell side exhibits a very slight rate of change during the first 10 μs of the deformation. This can be attributed to the low wave propagation speed in the specimen. Note that due to the low impedance of the foam specimens examined here, there would be an elapsed time between the instant at which the projectile hits the specimen and the time at which the compressive wave reaches the other end of the specimen,

i.e. the location of the load-cells. Therefore, the load-cells are not capable of recording the load exerted on the specimen during the early stages of deformation. During this early time period, the force applied on the projectile side of the specimen is significantly larger, resulting in significant deformation within the specimen, particularly within the regions close to the projectile (see Figure 8a). This non-equilibrium state gradually diminishes after t = 20 μs, resulting in the load magnitudes on the load-cell and projectile sides of the specimen becoming more equilibrated.

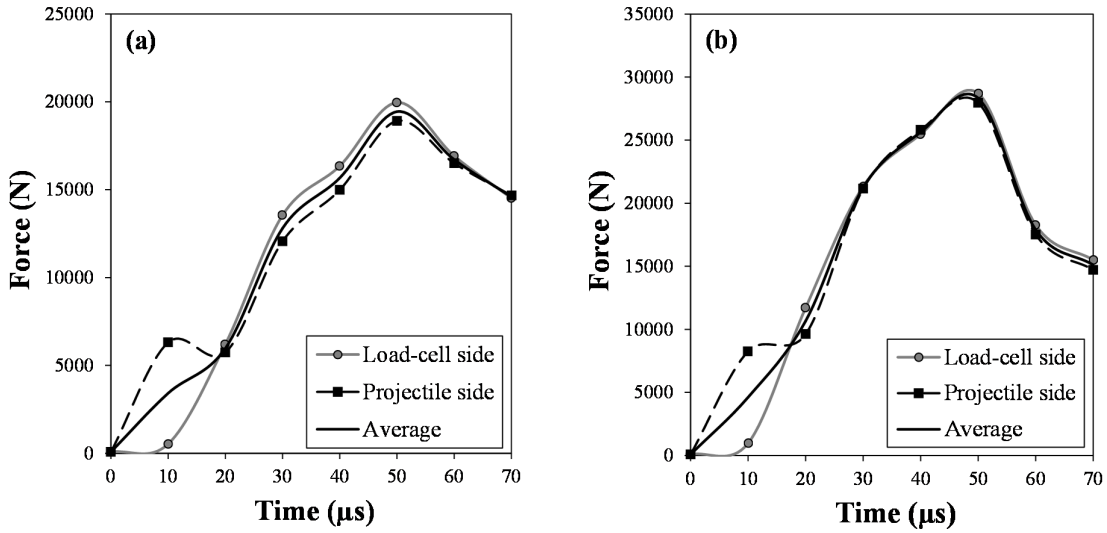

Fig. 15- Forces applied on the load-cell and projectile sides of the specimen for specimens deformed under (a) 1437 s^{-1} and (b) 2458 s^{-1} strain rate.

The non-equilibrium state of deformation that occurs during the early stages of impact can be studied through the stress-strain response of the specimen. Full-field axial strain and stress contours for the specimen subjected to 2458 s^{-1} strain rate are plotted in Figure 16. In this case also, the strain contours were obtained by slicing the specimen geometry into 25 thinner sections while averaging the strain values over each and every sliced section. The full-field strain data utilized for this purpose were those directly measured from DIC. Using the

previously obtained full-field acceleration and applying Eq. (18), the stress distribution was also obtained along the axis of the specimen. The stress-strain responses of the specimens are very similar to those described previously for the load history. The full-field contours shown in Figure 16 exhibit a highly non-homogeneous distribution of strain and stress during the first 20 μs of the deformation. For $t > 20\mu s$, the level of inhomogeneity in the deformation is substantially reduced and the specimen approaches homogeneity in the deformation state.

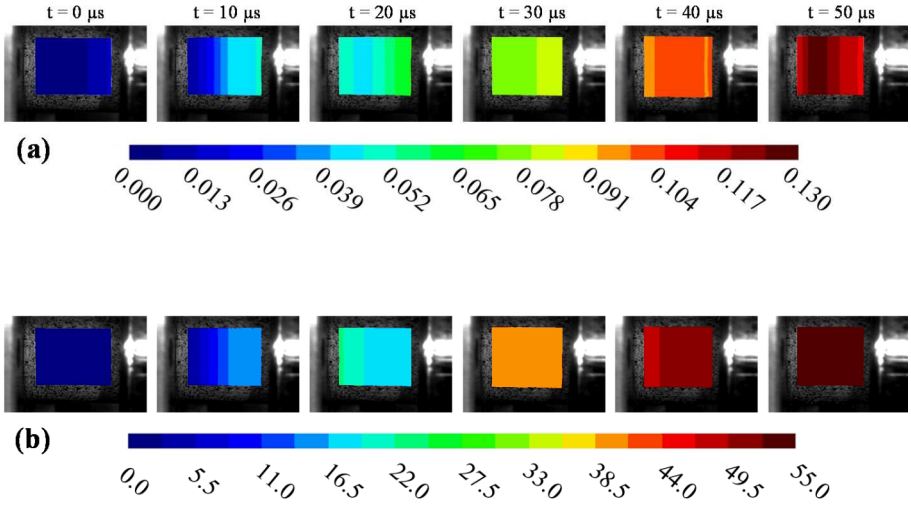

Fig. 16- full-field distribution of (a) axial strain and (b) axial stress (MPa) components for the specimen subjected to 2458 s^{-1} strain rate. Note that the strains and stresses are compressive in nature, but the values reported in here are the absolute values.

The significance of using the methodology outlined above is that the stress and strain histories within the material at any given position along its axis can be inversely calculated and studied, even when "dynamic equilibrium" conditions typically employed are not present. For instance, the evolution of strains and stresses extracted from different locations along the specimen axis are plotted in Figures 17 and 18, respectively. Similar to the load curves, remarkable differences between the local curves for both local strain and local stress

responses shown in Figures 17 and 18 are evident when $t < 20\mu s$. The local strain and stress curves obtained at different locations across the domain of interest were used to quantify and study the level of deformation heterogeneity in the specimens (Eqs. (19) and (20)). The stress (α_{σ_1}) and strain (α_{ε_1}) inhomogeneity coefficients were accordingly calculated and plotted in Figure 19. In line with the explanations provided earlier, both coefficients show significantly large values at $t < 40$ μs. The inhomogeneity coefficients take relatively lower values after this time, indicating that nominal "dynamic equilibrium" conditions for this material are present after a 40 μs delay time.

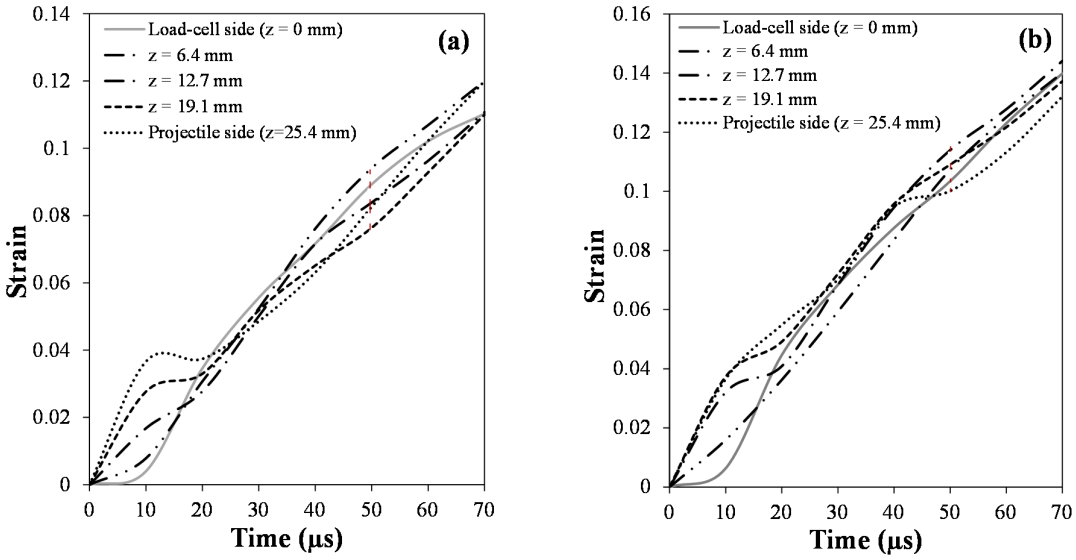

Fig. 17- Local strain evolutions extracted from different positions along the specimen axis for the foam specimens deformed at (a) 1437 s^{-1} and (b) 2458 s^{-1} strain rates.

Next, using the strain-time and stress-time curves obtained and shown earlier in Figures 17 and 18, the local stress-strain curves were determined. The local stress-strain curves for both strain rate conditions have been illustrated in Figure 20, where good agreement between each set of curves is indicated. Finally, the local stress-strain curves obtained at different positions

along the specimen axis were averaged and the resultant average curves were compared with the stress-strain response conventionally determined using the specimen-end force measurement. Note that in the conventional methodology, the strain was obtained by averaging the axial strain magnitudes, obtained directly from DIC, over the entire field of view. Consequently, only one strain value at each point of time is obtained in this method. Figure 21 compares the stress-strain curves using two methods, i.e. inverse analysis and the conventional method. It is clearly observed that by using the conventional methodology substantial error can be imposed on the results, making this method ineffective for the case of low impedance polymeric foams. In particular, the highest discrepancy between the curves is evident at earlier stages of deformation, as discussed in detail earlier.

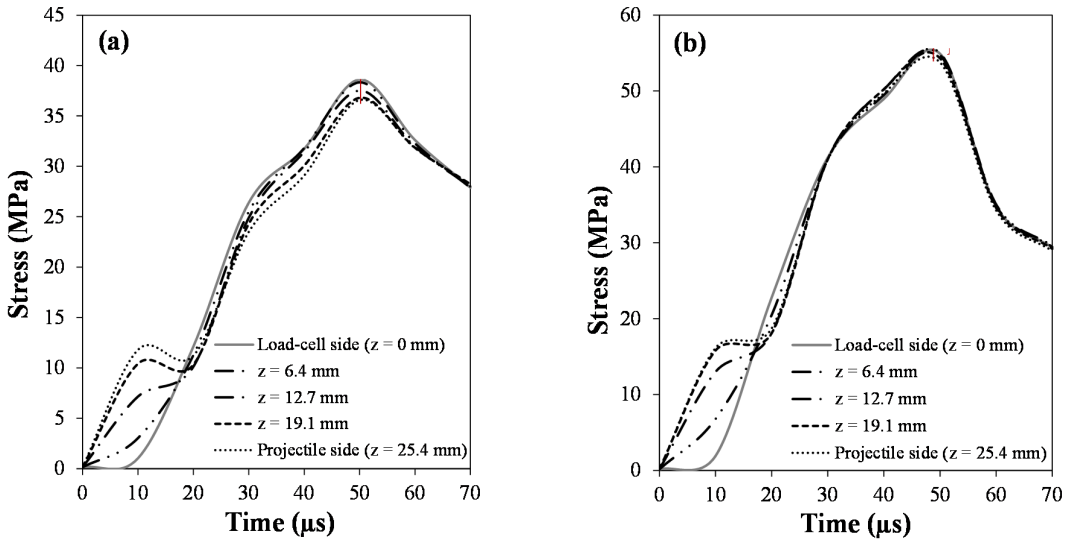

Fig. 18- evolution of local stress at different positions along the specimen axis for the foam specimens deformed at (a) 1437 s^{-1} and (b) 2458 s^{-1} strain rates.

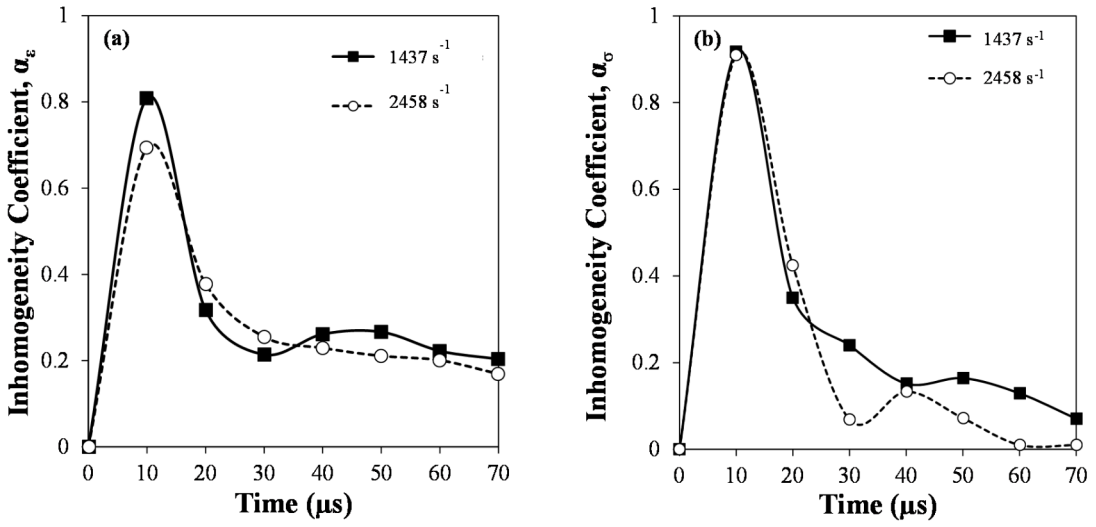

Fig. 19- Inhomogeneity coefficient for (a) strain (α_{ε_1}) and (b) stress (α_{σ_1}) as a function of time for both strain rate conditions.

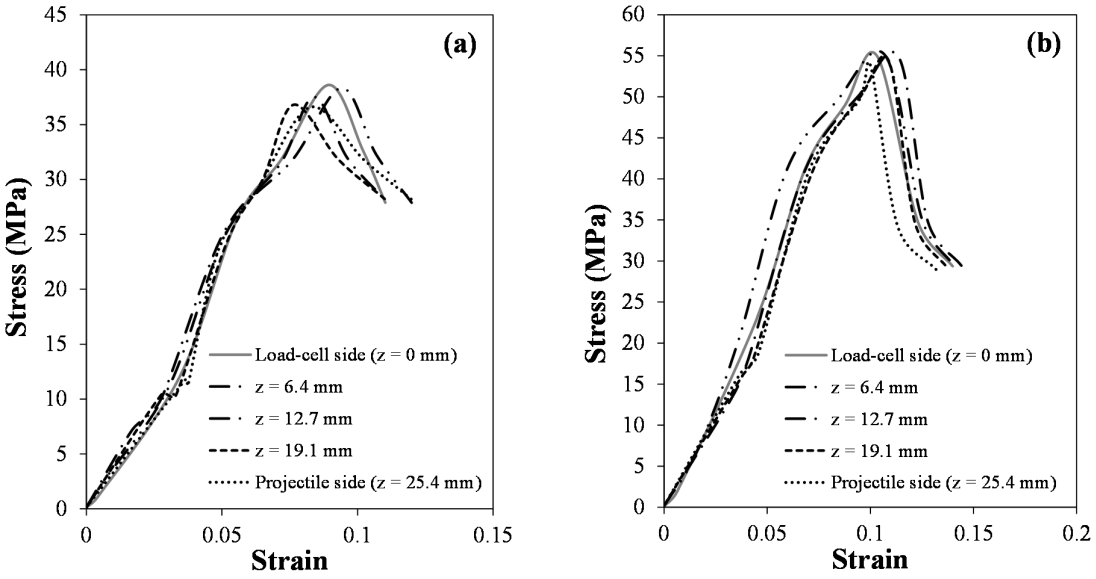

Fig. 20- Local stress-strain curves obtained at different positions along the specimen axis for the foam specimens deformed at (a) 1437 s^{-1} and (b) 2458 s^{-1} strain rates.

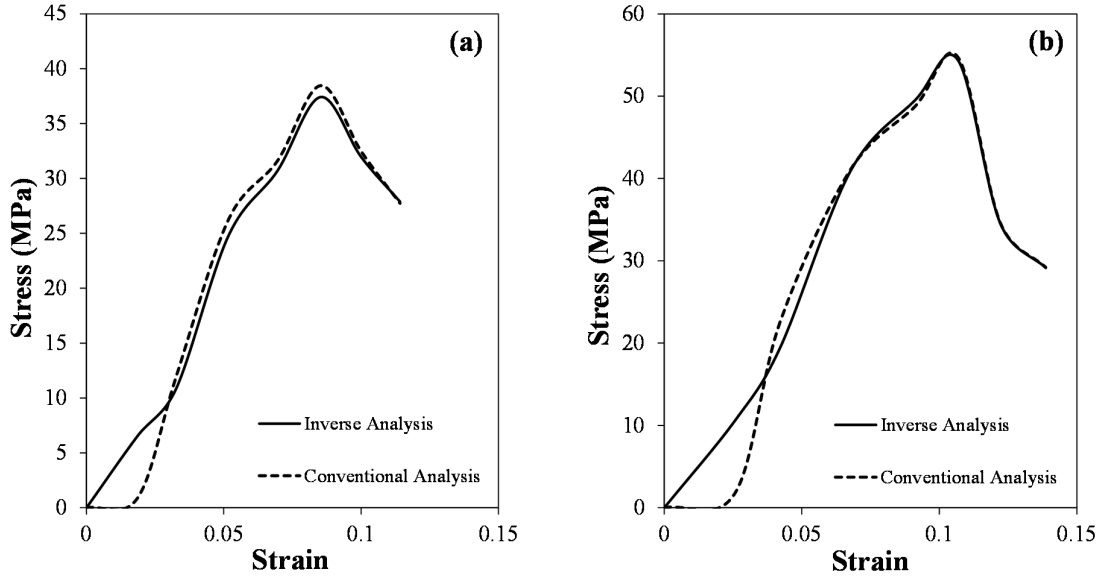

Fig. 21- Global stress-strain curves obtained using two different methods for foam specimens deformed at (a) 1437 s^{-1} and (b) 2458 s^{-1} strain rates.

5. Summary

One of the main challenges in the study of the deformation of materials at high strain rate conditions is the presence of non-equilibrium dynamic conditions. The issue deteriorates when dynamic constitutive behavior of soft and/or low impedance materials is to be investigated. For this case, the following are noted;

- It has been well established in the literature, and was clearly demonstrated in the present work, that conventional boundary measurements can introduce substantial error into the analysis.
- An inverse analysis was conducted in the present work which took advantage of full-field 3D digital image correlation measurements throughout the transient loading process to include the effects of compressibility and inertia forces and to overcome the limitations associated with conventional boundary measurements. The main

limitation present in the present work was the temporal resolution of the DIC measurements. This issue can be resolved by using ultra high speed cameras commercially available today.

- Attempts were made to include the concurrent influences of material compressibility and inertia effect in the analyses. Although the material examined here shows minimal change of density, the analysis can be applied to any low-impedance compressible solids, regardless of the degree of compressibility.
- The authors believe that following the procedure detailed in this work, it would be possible to carry out high strain rate experiments on low impedance and/or soft materials and extract accurate stress-strain relations, a concept that continues to be of great interest in the experimental mechanics' community.
- Clearly, the effort in this work was to demonstrate the applicability of the utilized inverse analysis. The authors believe that using this method, along with more powerful photography techniques and more advanced dynamic experiment apparatuses, the rate dependent elastic constants of materials, regardless of their high or low impedance characteristics can be obtained. This would be basically achieved following the improvement of ultra-high speed imaging techniques in the near future.

6. Conclusions

The dynamic stress-strain response of closed-cell rigid polyurethane foam was investigated using high speed photography with 3D digital image correlation. Owing to the low wave propagation speed of the examined foam specimens, a highly non-homogeneous state of deformation was observed during impact loading, conditions that require the inclusion of inertia stresses in the analysis. The change in density, inertia forces and stresses were first calculated using the full-field strain and acceleration distributions. By superimposing the

locally developed inertia stresses to the stress magnitudes measured at specimen end, the full-field distribution of axial stress developed within the material was inversely calculated. It was shown that the influence of inertia stresses is more pronounced during the earlier stages of deformation, thus making the conventional end measurements inaccurate during this transient time period and requiring the inclusion of inertia stresses in the analysis. The methodology detailed in this work was shown to be fully capable of predicting the local stress-strain response of low-impedance materials subjected to impact loading.

Acknowledgments

Sandia National Laboratories is a multi-program laboratory managed and operated by Sandia Corporation, a wholly owned subsidiary of Lockheed Martin Corporation, for the U.S. Department of Energy's National Nuclear Security Administration under contract DE-AC04-94AL85000.

References

[1] Field JE, Walley SM, Proud WG, Goldrein HT, Siviour CR. Review of experimental techniques for high rate deformation and shock studies. Int J Impact Eng 2004; 30: 725-775.

[2] Hopkinson B. A method of measuring the pressure produced in the detonation of high explosives or by the impact of bullets. Phil Trans R Soc Lond 1914; 213: 437-456.

[3] Song B, Chen W. Dynamic stress equilibrium in split Hopkinson pressure bar tests on soft materials. Exp Mech 2004; 44: 300-312.

[4] Mallon S, Kidane A, Lu WY. Full-field deformation observation of polymer foam subjected to shock loading. In: Song B, Casem D, Kimberley J (Editors), Dynamic behavior of materials – Volume 1, Proceedings of the 2014 Annual Conference on Experimental and Applied Mechanics, Springer, 2015, pp 83-89. DOI 10.1007/978-3-319-06995-1_14

[5] Othman R, Aloui S, Poitou A. Identification of non-homogeneous stress fields in dynamic experiments with a non-parametric method. Polym Test 2010; 29: 616-623.

[6] Aloui S, Othman R, Poitou A, Guegan P, El-Borgi S. Non-parametric identification of the non-homogeneous stress in high strain-rate uni-axial experiments. Mech Res Commun 2008; 35: 392-397.

[7] Zhang X, Zhang H. Optimal design of functionally graded foam material under impact loading. Int J Mech Sci 2013; 68: 199-211.

[8] Avalle M, Belingardi G, Montanini R. Characterization of polymeric structural foams under compressive impact loading by means of energy-absorption diagram. Int J Impact Eng 2001; 25: 445-472.

[9] Ouellet S, Cronin DS, Moulton J, Petel EO. High rate characterization of polymeric closed-cell foams: Challenges related to size effects. In: Chalivendra V, Song B, Casem D (Editors), Dynamic behavior of materials – Volume 1, Proceedings of the 2012 Annual Conference on Experimental and Applied Mechanics, Springer, 2013, pp 21-28. DOI 10.1007/978-1-4614-4238-7_4

[10] Petel OE, Ouellet S, Frost DL, Higgins AJ. Shock Hugoniot measurements in foam. J Phys: Conf Ser 2014; 500: 1-6.

[11] Viot P, Beani F, Lataillade JL. Polymeric foam behavior under dynamic compressive loading. J Mater Sci 2005; 40: 5829-5837.

[12] Flores-Johnson EA, Li QM. Low velocity impact on polymeric foams. J Cell Plast 2011; 47: 45-63.

[13] Linul E, Marsavina L, Voiconi T, Sadowski T. Study of factors influencing the mechanical properties of polyurethane foams under dynamic compression. J Phys: Conf Ser 2013; 451: 1-6.

[14] Ouellet S, Cronin D, Worswick M. Compressive response of polymeric foams under quasi-static, medium and high strain rate conditions. Polym Test 2006; 25: 731-743.

[15] Whisler D, Kim H. Experimental and simulated high strain dynamic loading of polyurethane foam. Polym Test 2015; 41: 219-230.

[16] Liu J, Saletti D, Pattofatto S, Zhao H. Impact testing of polymer foam using Hopkinson bars and digital image analysis. Polym Test 2014; 36: 101-109.

[17] Song B, Chen W. Dynamic stress equilibrium in split Hopkinson pressure bar tests on soft materials. Exp Mech 2004; 44: 300-312

[18] Oullet S, Cronin D, Worswick M. Compressive response of polymeric foams under quasi-static, medium and high strain rate conditions. Polym Test 2006; 25: 731-743.

[19] Chen R, Huang S, Xia K, Lu F. A modified Hopkinson bar system for testing ultra-soft materials under intermediate strain rates. In: DYMAT-International Conference on the Mechanical and Physical Behaviour of Materials under Dynamic Loading, vol. 1, pp. 389-394. EDP Sciences, 2009. DOI: 10.1051/dymat/2009055

[20] M.A Sutton, J.J Orteu, H.W Schrier. Image correlation for shape, motion and deformation measurements. Springer. NY. 2009

[21] Pierron F, Zhu H, Siviour C. Beyond Hopkinson's bar. Phil Trans R Soc A 2014; 372: 20130195.

[22] Gilat A, Schmidt TE, Walker AL. Full field measurement in compression and tensile split Hopkinson bar experiments. Exp Mech 2009; 49: 291-302.

[23] Koohbor B, Mallon S, Kidane A, Sutton MA. A DIC-based study of in-plane mechanical response and fracture of orthotropic carbon fiber reinforced composites. Compos Part B-Eng 2014; 66: 388-399.

[24] Mallon S, Koohbor B, Kidane A, Sutton MA. Fracture behavior of prestressed composites subjected to shock loading: A DIC-based study. Exp Mech 2015; 55: 211-225.

[25] Pierron F, Forquin P. Ultra-high-speed full-field deformation measurements on concrete spalling specimens and stiffness identification with the virtual fields method. Strain 2012; 48: 388-405.

[26] Moulart R, Pierron F, Hallett SR, Wisnom MR. Full-field strain measurement and identification of composites moduli at high strain rate with the virtual fields methods. Exp Mech 2011; 51: 509-536.

[27] Lu WY. Mechanical characterization of rigid polyurethane foams. Sandia Report 2014: SADN2014-20708.

[28] Mallon S, Koohbor B, Kidane A. Fracture of pre-stressed woven glass fiber composite exposed to shock loading. In: Song B, Casem D, Kimberley J (Editors), Dynamic behavior of materials – Volume 1, Proceedings of the 2014 Annual Conference on Experimental and Applied Mechanics, Springer, 2015, pp 213-219. DOI 10.1007/978-3-319-06995-1_32

[29] Koohbor B, Mallon S, Kidane A, Lu WY. The deformation and failure response of closed-cell PMDI foams subjected to dynamic impact loading. Polym Test 2015; 44: 112-124.

[30] L.J Gibson, M.F Ashby. Cellular solids: Structure and properties. 2nd ed. Oxford. 1997

[31] S. K Samanta. Dynamic deformation of aluminum and copper at elevated temperatures. J Mech Phys Solids 1971; 19: 117.

Figure Captions

Fig. 1- (a) Typical speckled specimen with its corresponding grey scale histogram shown in (b).

Fig. 2- (a) The shock tube at its entirety, with the loading fixture shown in (b). The schematic of the shock tube muzzle and the pressure transducer are depicted in (c).

Fig. 3- The experimental setup including the shock tube and the stereovision camera system used in this work.

Fig. 4- The schematic view of a compressible cylindrical specimen subjected to axial loading.

Fig. 5- Schematic of a cylindrical specimen subjected to direct impact. The dynamic load is applied on the specimen from the projectile side.

Fig. 6- Schematic geometry of the specimen sliced into a finite number of thinner segments, used to calculate the inertia force and stress applied at each point across the specimen axis.

Fig. 7- Evolution of the average axial strain applied on the specimen as a functions of time, for two different number of Mylar sheets.

Fig. 8- full-field distribution of (a) axial and (b) radial strain components for the specimen subjected to direct impact with two Mylar sheets.

Fig. 9- full-field distribution of plastic Poisson's ratio, υ_p, for the specimen subjected to direct impact with two Mylar sheets.

Fig. 10- Local plastic Poisson's ratio, υ_p, of the specimens extracted from different positions along the axis of foam specimens deformed at (a) 1437 s^{-1} and (b) 2458 s^{-1} strain rates.

Fig. 11- Variation of the projectile displacement with time. Increasing the number of plastic diaphragms from one to two has resulted in a 35% increase in the velocity of the projectile.

Fig. 12- variation of local density as a function of deformation time, extracted from different positions along the axis of foam specimens deformed at (a) 1437 s^{-1} and (b) 2458 s^{-1} strain rates.

Fig. 13- full-field distribution of (a) axial displacment (mm) and (b) axial acceleration (m/s^2) for the specimen subjected to higher strain rate conditions.

Fig. 14- Variation of the axial acceleration averaged over the entire domain of interest with respect to time.

Fig. 15- Forces applied on the load-cell and projectile sides of the specimen for specimens deformed under (a) 1437 s^{-1} and (b) 2458 s^{-1} strain rate.

Fig. 16- full-field distribution of (a) axial strain and (b) axial stress (MPa) components for the specimen subjected to 2458 s^{-1} strain rate. Note that the strains and stresses are compressive in nature, but the values reported in here are the absolute values.

Fig. 17- Local strain evolutions extracted from different positions along the specimen axis for the foam specimens deformed at (a) 1437 s^{-1} and (b) 2458 s^{-1} strain rates.

Fig. 18- evolution of local stress at different positions along the specimen axis for the foam specimens deformed at (a) 1437 s^{-1} and (b) 2458 s^{-1} strain rates.

Fig. 19- Inhomogeneity coefficient for (a) strain (α_{ε_1}) and (b) stress (α_{σ_1}) as a function of time for both strain rate conditions.

Fig. 20- Local stress-strain curves obtained at different positions along the specimen axis for the foam specimens deformed at (a) 1437 s^{-1} and (b) 2458 s^{-1} strain rates.

Fig. 21- Global stress-strain curves obtained using two different methods for foam specimens deformed at (a) 1437 s^{-1} and (b) 2458 s^{-1} strain rates.